IEEE Access
Multidisciplinary ⋮ Rapid Review ⋮ Open Access Journal

Received September 13, 2021, accepted November 17, 2021, date of publication November 22, 2021,
date of current version December 3, 2021.

Digital Object Identifier 10.1109/ACCESS.2021.3129927

Cost Minimization of a Permanent Magnet Eddy Current Brake by Multiobjective Particle Swarm Optimization Based on Nonlinear Reluctance Network Modeling

MEHMET GULEC[1,2], (Member, IEEE), PIA LINDH[3], (Senior Member, IEEE), METIN AYDIN[4], (Senior Member, IEEE), AND JUHA PYRHÖNEN[3], (Senior Member, IEEE)

[1]Department of Electromechanical, Systems and Metal Engineering, Ghent University, 9000 Ghent, Belgium
[2]Flanders Make@UGent—Corelab EEDT-MP, 3001 Leuven, Belgium
[3]Laboratory of Electric Drives Technology, LUT University, 53851 Lappeenranta, Finland
[4]Department of Mechatronics Engineering, Kocaeli University, İzmit, 41380 Kocaeli, Turkey

Corresponding author: Mehmet Gulec (mehmet.gulec@ugent.be)

This work was supported in part by the Finnish National Agency for Education (CIMO).

ABSTRACT Design optimization of a permanent magnet eddy current brake (PM-ECB) is performed by applying multiobjective particle swarm optimization (MO-PSO) for cost minimization. A previously designed and patented PM-ECB is used as a reference model in the study. A quasi-3-dimensional (3D) analytical modeling approach based on a reluctance network considering the actual structure of the reference PM-ECB is proposed and verified. The Gauss–Seidel method is used as a nonlinear solver for the reluctance network modeling, and the braking torque is calculated considering both the skin effect and the armature reaction. Multiobjective optimization is developed by applying a particle swarm algorithm, and a 3D Pareto front is provided to demonstrate all non-dominating design points. Three cost functions, viz. rated braking torque, magnet mass, and magnetic flux density of the yoke, are selected as the objectives for the optimization problem, and the optimum design point is addressed in detail. The optimized design is validated by 3D-FEA and experiments. The results indicate that a 40% reduction in the magnet volume could be brought about by the optimized PM-ECB design with practically the same braking torque. Further, a 40% cost reduction in the optimized brake could be achieved compared with the reference one.

INDEX TERMS Eddy current, eddy current brake, magnetic equivalent circuit, multiobjective optimization, nonlinear analysis, pareto front, particle swarm algorithm, permanent magnet eddy current brake, reluctance network modeling.

I. INTRODUCTION

Eddy current brakes (ECBs) represent a well-known, traditional technology still widely applied in a variety of applications. Because of their contactless structure, eddy current brakes have been proven to be reliable, and they can replace complex mechanical structures with a simpler design and construction. Eddy current braking technology is successfully implemented in various applications, such as industrial tools and roller coasters, and in transportation, for instance, trucks and trains [1]–[6].

The associate editor coordinating the review of this manuscript and approving it for publication was Su Yan.

Contrary to electric machines, the aim of ECBs is to generate eddy-current-based braking force or torque in a conductive part of the brake. As a conductive part, a thin copper or aluminum cover is typically used in ECBs, especially in linear-type industrial products [7]–[9]. In addition, solid steels with magnetic and electrical properties are used in ECBs, particularly in axial-flux-type industrial products [10], [11]. Recent research on ECBs [25] has introduced a new fast calculation method for the braking torque and temperatures of ECBs. Permanent magnets (PMs) or excitation coils can be used as the magnetic field source in ECBs. In recent years, the excitation coils in the conventional designs have been replaced with PM-ECBs, which

provide more torque density, a smaller size, and easier implementation than conventional ECB designs [14]–[17]. The braking torque can also be increased by using a magnetic clad material [18]. Therefore, optimization of the PM-ECB is gaining in importance to achieve an efficient brake design. Optimization can be carried out by analytical or numerical approaches. Nevertheless, FEA-based optimization of an ECB would take several months even if only a few parameters were taken into account [19]. If there is a cost minimization problem, analytical optimization is essential in order to consider all the design parameters. However, analytical optimization requires very sensitive and detailed modeling. Thus far, an analytical approach to the optimization of a PM-ECB has not been provided in the literature. In addition, studies on the demagnetization risks of the PM-ECB have not been reported [14], [16], [17], [20].

In this study, a very sensitive and detailed quasi-3D analytical model is developed for the optimization problem, and the proposed analytical model is verified by 3D-FEA and experimental results. Linearization of the actual shape of the PM geometry, the armature reaction, and the demagnetization issue are all examined in the study. The objective of this paper is to develop a new low-cost design for a previously designed and patented PM-ECB used in a roller blind product. The design is accomplished by considering multi-conflict objectives and using a particle swarm algorithm. The contributions of this paper are (1) the development of a simple and fast analytical modeling approach, which meets the requirements of the application and (2) its implementation into a nonlinear optimization problem for developing a superior design for an actual eddy current brake.

The paper is structured as follows: The reference PM-ECB is addressed in detail in the first section. The 2D nonlinear reluctance network modeling is described, and a quasi-3D analytical approach is proposed in Section III. In the next section, multiobjective particle swarm optimization (MO-PSO) is provided with constant, variable, and target parameters, and the optimized design is presented by a 3D Pareto front profile. Finally, verification and comparison of the optimized PM-ECB is performed by applying the FEA.

II. REFERENCE PERMANENT MAGNET EDDY CURRENT BRAKE

The study was carried out in close cooperation with a roller blind manufacturer, using the dimensions of actual industrial products. A patent has been granted for the application [1]. The reference model was previously designed for a curtain company located in Finland. The company sells roller blinds with four different diameters (from 25 mm to 40 mm) and three different weights. The weights of the blinds are 1.5 kg (light), 3 kg (medium), and 5 kg (heavy). The required drag force and the suitable speed vary according to the roller blind. The most sold brake type for roller blinds was selected as the reference model prototype. According to the measurements of the roller blind, a smooth drag force was calculated at 0.65 m/s, which corresponds to a rotational speed

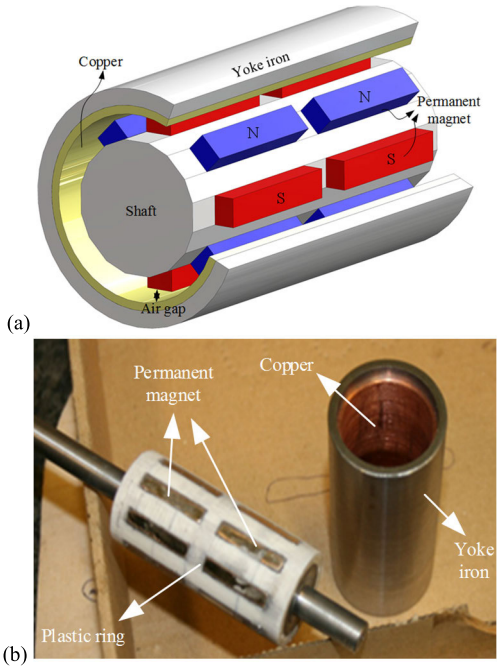

FIGURE 1. (a) 3D view of the reference PM-ECM and (b) photo of the prototype.

of 300 min^{-1}, and the length required for the ECB of the roller blind was calculated to be 40 mm by [21]

$$T = S\sigma_{F\tan}r \tag{1}$$

where T is torque, S is the active rotor surface area, r is the radius of the air gap, and $\sigma_{F\tan}$ is the tangential stress, which was assumed to be 1.5 kPa according to the outer diameter of the blind.

The materials for the reference PM-ECB were selected to be easily available standard materials with standard dimensions. The permanent magnet grade N48 was chosen for the prototype. This material has a remanence flux density from 1.37 to 1.42 T and a coercive field strength $\geq$ 955 kA. A 3D view of the reference PM-ECB and a photo of the prototype are given in fig. 1. The reference PM-ECB has eight poles, and two PM stacks are used to get the total active axial length. The benefit of using two PM stacks is the easy assembly in automatic production as the magnets are placed in a plastic support. The key parameters of the reference PM-ECB are given in Table 1. The outer diameter of the reference PM-ECB is 32.6 mm, and its total axial length is 55 mm. The dimensions of one piece of the permanent magnet are $4 \times 3 \times 20$ mm^3, and the total PM mass in the reference PM-ECB is 28.8 g.

The reference PM-ECM was first investigated by the 2D-FE method to demonstrate the structure and the operating principle in short. The 2D-FEA model with a mesh profile is shown in Fig. 2(a) to illustrate the structure of the reference PM-ECB. The Altair Flux v11.3 software was used in the FEA simulations. The symmetry model was taken into account, and the magnetic flux density and current density profiles at the speed of 330 min^{-1} are given in Fig. 2(b)–(c),

TABLE 1. Key parameters of the reference PM-ECB.

Rated speed,	330 min^{-1}	Outer diameter	32.6 mm
Mechanical air gap, g	0.5 mm	Yoke thickness	2.3 mm
Tot. axial PM length, l_{stk}	40 mm	Copper thickness, h_{Cu}	1.17 mm
Total PM mass	28.8 g	PM dimension	4×3×20 mm^3

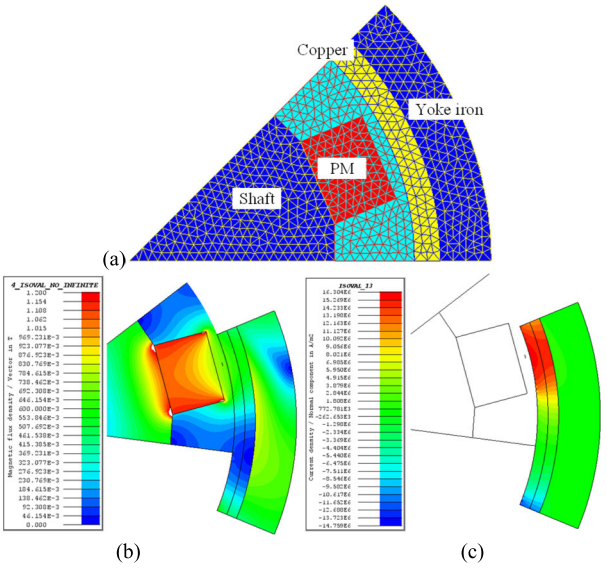

FIGURE 2. 2D-FE symmetry model of the reference PM-ECB: (a) mesh structure, (b) magnetic flux density profile, and (c) current density profile at the speed of 330 min^{-1}. The figure (b) indirectly shows that eddy currents occur also in the iron even though they are not clearly visible in (c) with this scaling.

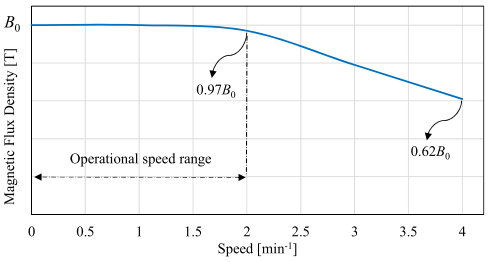

FIGURE 3. Variation in the average air-gap normal magnetic flux density B_n as a function of speed for the reference PM-ECB obtained from (2) and (3).

respectively. The figure shows that the maximum magnetic flux density in the yoke is 0.7 T, and the maximum current density in the copper is 16.3×10^6 A/m^2.

The operational speed range of the reference PM-ECB varies from 105 to 1150 min^{-1}. It is pointed out that the armature reaction occurs naturally in ECBs, and it should be investigated as

$$B_n = B_0 e^{-R_m} \tag{2}$$

where B_n is the normal magnetic flux density, B_0 is the magnetic flux density at zero speed, and R_m is the magnetic Reynolds number defined as [20]

$$R_m = \frac{v_c}{\rho_{Cu}} \mu_0 l_c \tag{3}$$

where v_c is the characteristic velocity $v_c = \omega r_{Cu}/p$ where ω is the electrical angular speed, r_{Cu} is the copper air gap surface radius and p is the number of pole pairs, ρ_{Cu} is the copper resistivity, μ_0 is the vacuum permeability, and l_c is the characteristic length given by the copper volume V_{Cu} divided by its air gap surface S_{Cu} ($l_c = V_{Cu}/S_{Cu}$). Fig. 3 shows the change in the magnetic flux density as a function of speed for the reference PM-ECB by (2) and (3). 2D-FEAs were also carried out to verify the armature reaction obtained from (2) and (3). Air-gap flux density profiles of the reference PM-ECB at various speeds are given in Fig. 4. It can be seen that the magnetic flux density variation given by the 2D-FEA supports the analytical assumption.

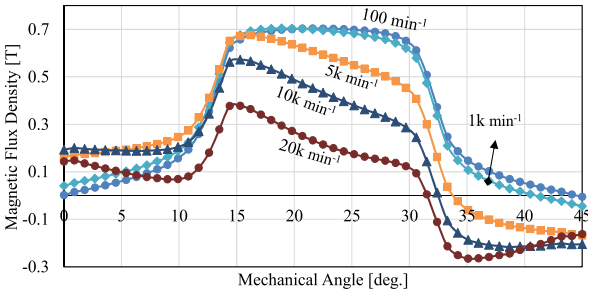

FIGURE 4. Normal air-gap flux density profiles of the reference PM-ECB at various speeds given by the 2D-FEA. A very high speed is needed to achieve a significant armature reaction.

III. NONLINEAR RELUCTANCE NETWORK MODELING OF THE PM-ECB

The magnetic flux density in the conductive regions should be accurately calculated to achieve a correct braking torque. In this paper, 2D nonlinear reluctance-network-based magnetic equivalent modeling is investigated as an analytical approach that enables a low-calculation-cost optimization process. The reluctance network model can be applied to various kinds of electric machines; in the case of the ECBs, the aim being to compute current density in the moving conductive region. The reluctance network modeling relies on a rectangular-element-based mesh structure over the entire model, and all the mesh structure elements have x- and y-axis reluctances in both the positive and negative directions. In the method, the mesh structure is determined by the complexity of the model. By the network model, all flux paths can be determined with a high precision, and predesign outputs can be quickly obtained [22], [23].

The reference PM-ECB has eight poles, and therefore, it can be modeled by a 1/8 symmetric model. A symmetric reluctance network model of the reference PM-ECB is given in Fig. 5. All nonmagnetic regions, such as copper, air gap, and PM, were modeled by two horizontal layers to increase the solution accuracy. There can also be more layers,

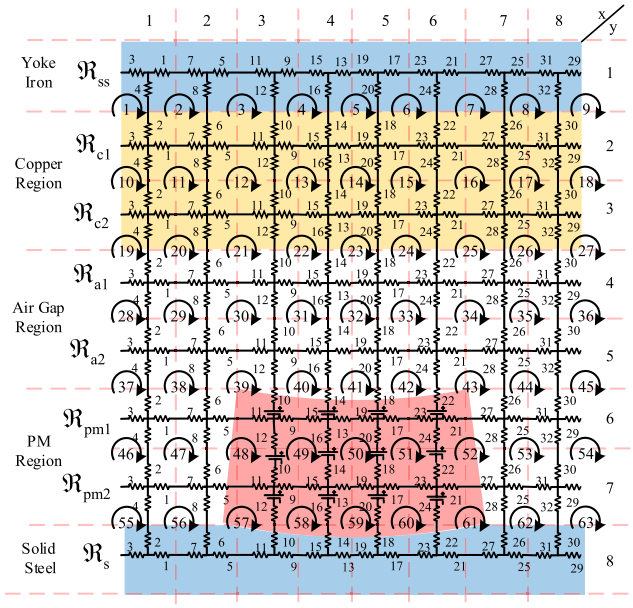

FIGURE 5. Symmetric 2D reluctance network model of the PM-ECB considering a flat-shaped PM.

but considering the armature reaction and the computational effort, a two-layer model was preferred. In total, a 7-to-9 mesh structure was developed for the symmetry model.

It is important to consider the actual flat-shaped PM geometry in the 2D nonlinear reluctance network model as the PM geometry plays a critical role in the brake performance. The actual flat-shaped PM geometry is linearized, and a variable air-gap structure is obtained by applying an arc-shaped trapezoid PM geometry, which has cylindrical reluctances defined as [23]

$$\Re_x = \frac{1}{\mu_0 \mu_{\text{pm}}} \frac{\alpha}{\log\left(\frac{r_{\text{PM}}}{r_{\text{shaft}}}\right) d} \tag{4}$$

$$\Re_y = \frac{1}{\mu_0 \mu_{\text{pm}}} \frac{1}{\alpha d} \log\left(\frac{r_{\text{PM}}}{r_{\text{shaft}}}\right) \tag{5}$$

where μ_{pm} is the relative permeability of the PM, α is the PM angular width, d is the axial length, r_{PM} is the radius of the PM, and r_{shaft} is the shaft radius. After calculating the PM cylindrical reluctances, the sub-reluctances related to the mesh structure are distributed. When the optimization process is considered, all variable design cases will be investigated, and this variable air-gap and trapezoid geometry will be dominant in some designs. A parametric study was performed to examine the arc-shaped trapezoid PM geometry. The braking torque profiles obtained from the rectangular PM geometry, and the arc-shaped trapezoid geometry are given in Fig. 6. It can be seen that the difference between the two geometries is greatly increased when the PM width increases, which is unacceptable. Therefore, considering the actual flat-shaped PM geometry is vital for the analytical approach.

MATLAB® software was used to develop the network model and nonlinear analyses. All the reluctances, meshes, and current linkages were created automatically with loops

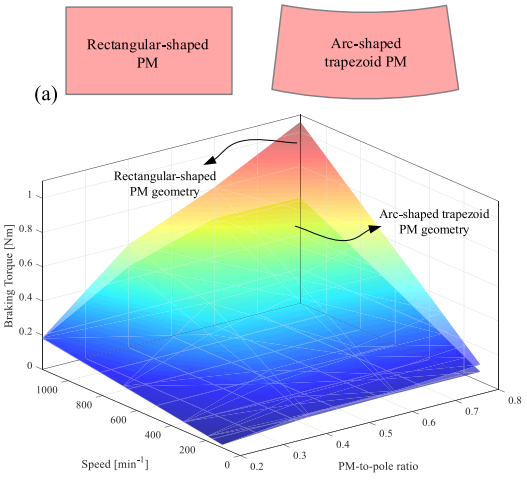

FIGURE 6. Comparison of the braking torque profiles: a) rectangular-shaped and arc-shaped trapezoid PM geometries and b) braking torque profiles under consideration.

after determining the variables. The size of the 63 × 63 main reluctance matrix, the size of the 1 × 63 current linkage matrix, and the flux matrix related to the rectangular-based meshes are defined as

$$\begin{bmatrix} \varphi_1 \\ \varphi_2 \\ \varphi_3 \\ \vdots \\ \varphi_{63} \end{bmatrix} = \begin{bmatrix} \Re_1 & \Re_{1-2} & \Re_{1-3} & \cdots & \Re_{1-63} \\ \Re_{2-1} & \Re_2 & \Re_{2-3} & \cdots & \Re_{2-63} \\ \Re_{3-1} & \Re_{3-2} & \Re_3 & \cdots & \Re_{3-63} \\ \vdots & \vdots & \vdots & \ddots & \vdots \\ \Re_{63-1} & \Re_{63-2} & \Re_{63-3} & \cdots & \Re_{63} \end{bmatrix}^{-1} \begin{bmatrix} \Im_1 \\ \Im_2 \\ \Im_3 \\ \vdots \\ \Im_{63} \end{bmatrix} \tag{6}$$

where φ is the flux, $\Re$ is the reluctance, and $\Im$ is the current linkage. The subscripts of the parameters represent the related fluxes and their adjacent fluxes (only for reluctances). For example, $\Re_{2-3}$ is defined as

$$\Re_{2-3} = \Re_{\text{ss}}(8) + \Re_{\text{c1}}(6) \tag{7}$$

Nonlinear analysis is required, because the yoke is made from solid steel and, naturally, entails an eddy-current reaction. In addition, a sensitive model is essential for the optimization problem. A low-carbon steel [24] was used in solid steel parts, and the resistivity of the yoke was taken as 25×10^{-8} Ω·m. The Gauss–Seidel method with relaxation was preferred for the 2D reluctance network model. The flowchart of the nonlinear method for the 2D reluctance network model is given in Fig. 7. The nonlinear method consists of two Gauss–Seidel stages so that the main iteration calculates the magnetic flux densities and updates the *BH* curve. In the sub-iteration, the fluxes are updated and calculated by solving (6). The investigated nonlinear method is much less time-consuming than the single iteration (conventional) approach. In the MATLAB software, the single-iteration Gauss–Seidel method took 9.8 s, whereas the method under study took only 6.1 s. When any optimization process is considered, less time-consuming computations play a critical role. All the required errors (ε) in the Gauss–Seidel method

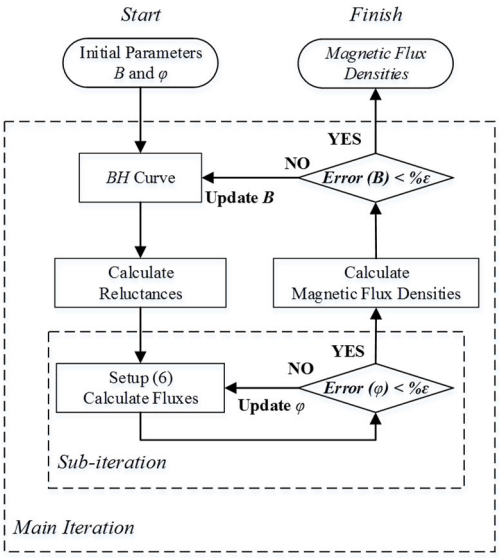

FIGURE 7. Flowchart of the nonlinear method for the 2D reluctance network model.

were set to 0.0001%, and a relaxation factor of 0.5 was used in the design.

Because of the overhang structure of the reference PM-ECB, the analytical approach should be improved to achieve correct results in practice. The 3D magnetic flux density profiles produced by the analytical and 3D-FEA approaches are given in Fig. 8 to demonstrate the difference. It is clearly seen that the analytical approach does not match the actual 3D model. In this paper, the effect of the overhang was taken into account by the well-known Carter's theory [26]. The magnetic thicknesses of the nonmagnetic regions (air gap and copper) are expressed by magnetic equivalents as

$$g_{k_C} + h_{Cuk_C} = (g + h_{Cu})k_C \tag{8}$$

where g is the air gap, h_{Cu} is the copper thickness, and k_C is Carter's factor defined as

$$k_C = \frac{t_1}{t_1 - y_1(g + h_{Cu})} \tag{9}$$

where t_1 is the slot pitch defined as

$$t_1 \approx 2l_{oh} + 0.5l_{stk} \tag{10}$$

where l_{oh} is the axial overhang length, and l_{stk} is the total axial PM length. The factor of y_1 in (9) is defined as

$$y_1 = \frac{4}{\pi}\left(\frac{2l_{oh}}{2g}\arctan\left(\frac{2l_{oh}}{2g}\right) - \ln\sqrt{1 + \left(\frac{2l_{oh}}{2g}\right)^2}\right) \tag{11}$$

The nonlinear 2D reluctance network model is modified with (8)–(11), and a quasi-3D analytical reluctance network model is achieved. The most important benefit of the quasi-3D analytical approach is the simple and accurate calculation of the braking torque. The following steps are taken to obtain the braking torque:

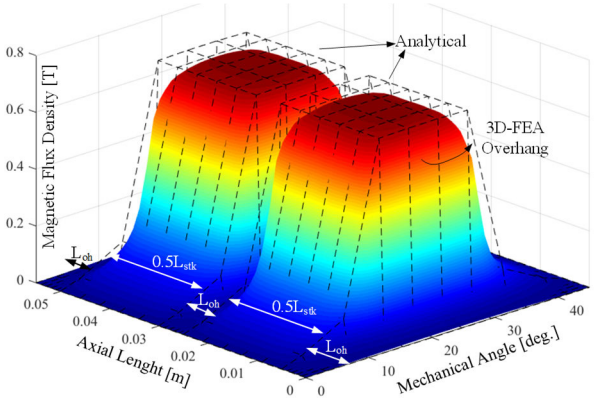

FIGURE 8. 3D Magnetic flux density profile of the reference PM-ECB in the middle of the air gap given by the analytical and 3D-FEA considering overhang.

- Calculate the magnetic flux density for all vertical reluctances in the copper and yoke regions (no contribution by circumferential reluctances. According to Lorentz force a particle charge dQ moving with a velocity in magnetic field density experiences a force dF = dQ $v \times B$).
- Update the magnetic flux densities with the armature reaction by applying (2) and (3).
- Calculate the current density separately for all the related reluctances defined as

$$J = \sigma(r\omega \times B_n)e^{(h/\delta)} \tag{12}$$

where h is the thickness and δ is the skin depth written as [27]

$$\text{for copper } \delta = \sqrt{\frac{2}{\sigma\omega\mu_0\mu_r}}$$
$$\text{for yoke } \delta = \sqrt{\frac{2H_0}{\sigma\omega B_s}} \tag{13}$$

where μ_r is the magnetic permeability of the conductive part, H_0 is the peak value of the applied surface magnetic field strength, and B_s is the saturation value of the magnetic flux density. For saturating materials, if a time-varying magnetic field is applied to the conductive region, the magnetic flux density will be either $-B_{st}$ or $+B_{st}$ [27]. It is pointed out that if the skin depth is greater than the related thickness, the factor of $e^{(h/\delta)}$ is neglected in the analysis.

- Calculate power for all the related reluctances considering their radius, defined as

$$P_{Cu} = \rho J^2 V_{Cu} \tag{14}$$

where V_{Cu} is the volume of the conductive part.

- Calculate the braking torque for each reluctance as below and sum

$$T_{br} = \frac{P_{Cu}}{\omega} \tag{15}$$

To validate the proposed quasi-3D analytical modeling, several design cases were evaluated, and the results were compared with the 3D-FEA. Details of the design cases are

given in Table 2. It can be seen that the quasi-3D analytical approach works as expected.

TABLE 2. Various design cases for validation of the Quasi-3D analytical modeling.

	Reference	v1	v2	v3
Total PM mass [g]	28.8	28.8	28.8	28.8
PM-to-pole ratio	0.41	0.6	0.2	0.5
Pole number	8	12	16	4
Copper thickness [mm], h_{Cu}	1.17	1.17	2	0.5
Braking torque at 330 min^{-1}				
Quasi-3D Analytical [Nm]	0.144	0.159	0.6	0.128
3D-FEA [Nm]	0.142	0.157	0.59	0.135

IV. MULTIOBJECTIVE DESIGN OPTIMIZATION OF THE PM-ECB BY A PARTICLE SWARM ALGORITHM

A. PARTICLE SWARM ALGORITHM

Because of its simple and effective structure, the particle swarm algorithm was selected for the multiobjective optimization [28], [29]. The particle swarm algorithm is a metaheuristic optimization method, which is inspired by the social behavior of bird flocking and fish schools. In the PSO, all particles share their experiences with the population (swarm), and each particle updates its position (x) and velocity (υ) by personal (*pbest*) and global (*gbest*) best solutions. The particle swarm algorithm can be explained by only two equations defined as

$$\upsilon_i^{k+1} = \xi_{iw}\upsilon_i^k + c_1 r_1\left(pbest_i^k - x_i^k\right) + c_2 r_2\left(gbest_i^k - x_i^k\right) \quad (16)$$

$$x_i^{k+1} = x_i^k + \upsilon_i^{k+1} \quad (17)$$

where k is the iteration number, i is the particle index, ξ_{iw} is the inertia weight, c_1 and c_2 are the personal and global acceleration coefficients, and r_1 and r_2 are randomly generated numbers between 0 and 1. In the PSO, ξ_{iw} is taken as 0.5, and its damping rate, which is the reduction rate from one iteration to the next, is taken as 0.99. The coefficients of c_1 and c_2 are taken as 1 and 2, respectively.

The flowchart of the particle swarm algorithm is given in Fig. 9. The particle swarm algorithm is an iterative process where the optimization starts with problem definition and PSO initialization. In the PSO initialization, the positions and velocities of particles are randomly created. The initial values of *gbest* and *pbest* are taken as $+\infty$ or $-\infty$. This depends on the problem definition, that is, whether minimization or maximization is the task. After initialization, velocity and position are calculated for each particle, respectively, and the cost function is evaluated by particle position, which is a vector with values of the variables. After obtaining the cost function, *pbest* and *gbest* values are checked and updated if necessary. This loop is performed for all particles. Next, the optimization termination criteria are checked, and the process is repeated until the final number of iterations is reached. Finally, the *gbest* solution is assigned as the optimum design, and the optimum design parameters are obtained by the *gbest* position.

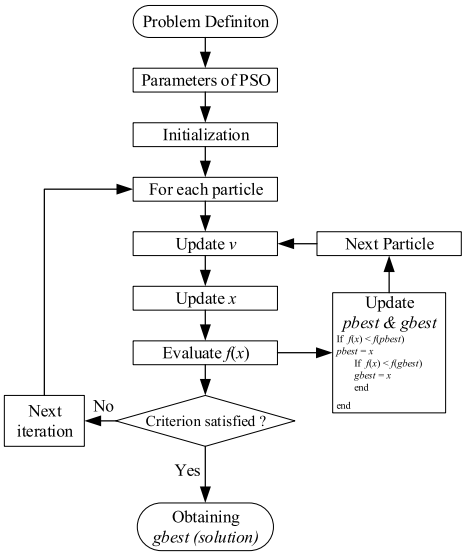

FIGURE 9. Flowchart of the particle swarm algorithm.

Generally, the weighting method is preferred for multiobjective optimization problems because of its simple structure and easy implementation. This method consists of only one cost function, which is the sum of the weighting objectives. The weighting is done in the order of importance. This method is easy to employ, but only one solution can be achieved and nondominant solutions cannot be found without modification, as it was shown in [30]. In this paper, all the objectives are evaluated independently and simultaneously in the optimization. In every iteration, *pbest* and *gbest* values are assigned from nondominated solutions in an external archive [29]. The external archive uses hypercubes to explore the search space for leader selection and a mutation operator to affect the particle behavior. At the end of the optimization, Pareto optimality is obtained by using the external archive in order to see all the nondominated design points. The proposed quasi-3D analytical modeling approach is implemented to the MO-PSO with 250 as the size of population and the repository size, and 100 as the number of iterations. This means that 25,000 design cases are evaluated to get an adequate Pareto front. Four design parameters (PM width-to-pole ratio, PM thickness, copper thickness, and steel thickness) are selected as variables. The maximum and minimum values of the variables are given in Table 3. As an industrial product, the PM-ECB has a specific geometry, and the geometric limitations determine the values of the variables.

For a fair comparison, the outer radius, the air gap, and the axial length of the total PM are fixed in the MO-PSO. The rated braking torque, PM volume, and yoke magnetic flux density are determined as cost functions. Exactly the same rated braking torque as in the first objective is used in the optimization, and the total PM mass (2nd objective) is targeted as the minimum for the cost reduction. The magnetic flux

TABLE 3. Variable parameters.

	Min. value	Max. value	Unit
PM-to-pole ratio	25%	65%	-
PM thickness	0.5	2	mm
Copper thickness, h_{Cu}	0.5	1.5	mm
Steel thickness	1	4	mm

density of the yoke (the third objective) is aimed at 1.2 T, which is the saturation point of the yoke material, to eliminate oversaturation and unexpected faults. The cost functions are defined as

$$f_1 = \min(|T_{\text{br}} - 0.146|) \tag{18}$$

$$f_2 = \min(\text{Total PM Mass}) \tag{19}$$

$$f_3 = \min(|\text{Yoke Magn. Flux Dens.} - 1.2|) \tag{20}$$

B. SENSITIVITY ANALYSIS

Before optimization, a sensitivity analysis is performed to describe the influence of the input parameters on the objective functions. 100 design of experiments (DOE) are created by a lattice sequence method, which aims to spread the designs equally in the design space. The analysis results are given in Fig. 10. The following conclusions are drawn from the sensitivity analysis:

- For the braking torque, PM thickness and the PM-to-pole ratio have a positive impact on the braking torque. The PM geometric parameters and the copper thickness have in total 90% of the total cumulative.
- For the PM mass, the design variables of the magnets are the most effective ones.
- For the magnetic flux density in the yoke, steel and copper thicknesses have a negative effect on the flux density and the major impact comes from the steel thickness.

C. 3D PARETO FRONT AND DISCUSSION

A 3D Pareto front obtained from the MO-PSO is given in Fig. 11. It should be noticed that the values of the first and third cost functions represent the absolute differences between the target value and the obtained value. The second cost function represents the actual value. For example, the magnetic flux density of the yoke in the reference model is 0.7 T, and the target value in the MO-PSO is 1.2 T (the third objective). Thus, there is an absolute difference of 0.5 T. In the figure, the red circles represent the nondominated solutions produced by roulette wheel selection, which is a genetic operator for selecting the possible solutions of the design cases [29]. The red triangle in the figure indicates the utopia design point, which is an unfeasible but a desirable design point, where all the cost functions attain their goals. The design point of the reference PM-ECB is also represented in the figure by a blue square. It is clearly seen from the Pareto front that there are many lower-cost design points than the reference design point. The selected design point, referred to as optimized design, is indicated by a black star in the figure. The reasons for the selection of this point are listed below:

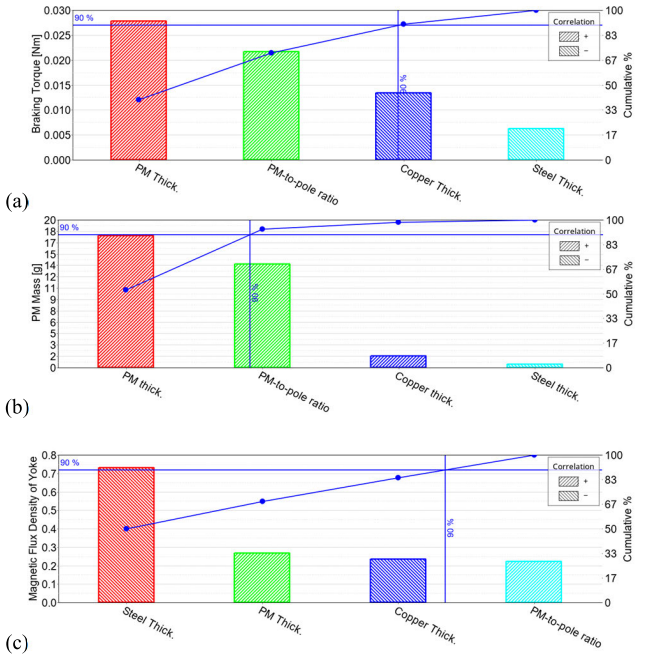

FIGURE 10. Sensitivity analysis of the input variables on (a) braking torque, (b) PM mass and (c) magnetic flux density of yoke.

- For the first objective: The rated braking torque is a key parameter, which should be kept the same with the reference model, and thus, the selected point should be very close to it.
- For the second objective: Cost reduction, similar to the rated braking torque, is the objective of this study. However, it is clearly seen from the Pareto front that the rated braking torque decreases with a decrease in the PM volume. Therefore, it is critical that the selection should be made by considering the rated braking torque.
- For the third objective: Efficient use of the yoke is also important; therefore, when the magnetic properties are considered, the aim is at approx. 1.2 T of magnetic flux density. In addition, it should be noted that the radius of the conductive part is also dominant in the braking torque.

V. OPTIMIZED PM-ECB

A. FEA AND COMPARISON

Comparison and verification of the optimized PM-ECB is vital to validate the proposed quasi-3D analytical modeling approach and the MO-PSO. A comparison of the normal and tangential components of the air-gap magnetic flux density profile for the reference and the optimized PM-ECB is given in Fig. 12. The figure shows that the normal and tangential components of the optimized model have a lower PM width-to-pole ratio with a lower magnetic flux density. The maximum normal magnetic flux density of 0.7 T is obtained by the reference, and 0.64 T by the optimized model. The results given by the analytical approach match the 3D-FEA.

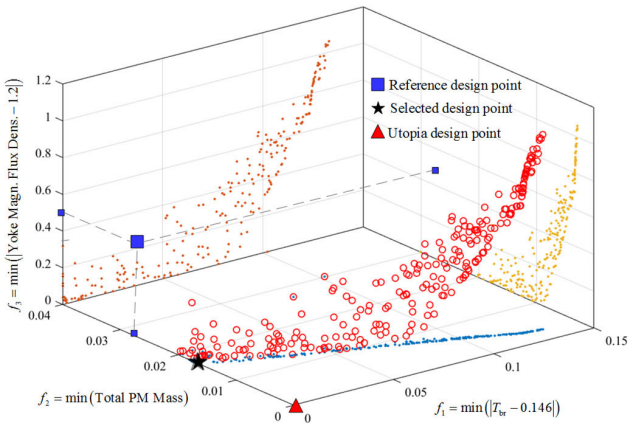

FIGURE 11. 3D Pareto front view obtained from the MO-PSO. The 1st objective is the braking torque. The 2nd objective is the total PM mass, and the 3rd objective is the yoke magnetic flux density.

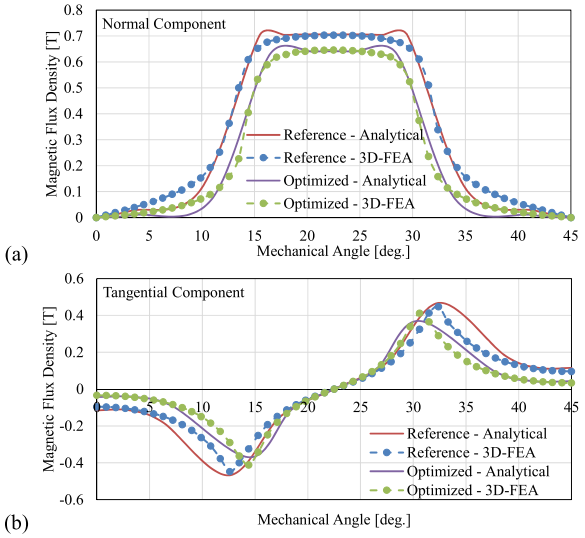

FIGURE 12. Comparison of the reference and the optimized PM-ECB: (a) normal and (b) tangential components of the magnetic flux density in the air gap with both the nonlinear reluctance network modeling and 3D-FEA approaches.

A series of simulations were carried out by the 3D-FEA for the validation. The magnetic flux density distributions of the reference and the optimized PM-ECB are illustrated in Fig. 13. It has to be borne in mind that the optimized PM-ECB has exactly the same air gap, outer radius, total PM axial length, and overhang structure as the reference model. The 2D views of the reference and the optimized PM-ECB are also given in the figure. The optimized PM-ECB has a lower PM width-to-pole ratio and less PM material than the reference PM-ECB. Moreover, an efficient use of the yoke was achieved by the optimized PM-ECB compared with the reference PM-ECB. Compared with the reference model, the 3D-FEA gave a maximum magnetic flux density of 1.18 T in the yoke, while the optimized quasi-3D analytical approach provided a value of 1.22 T. A detailed comparison of the reference model and the optimized PM-ECB is presented in Table 4. The results show that the optimized model yielded a

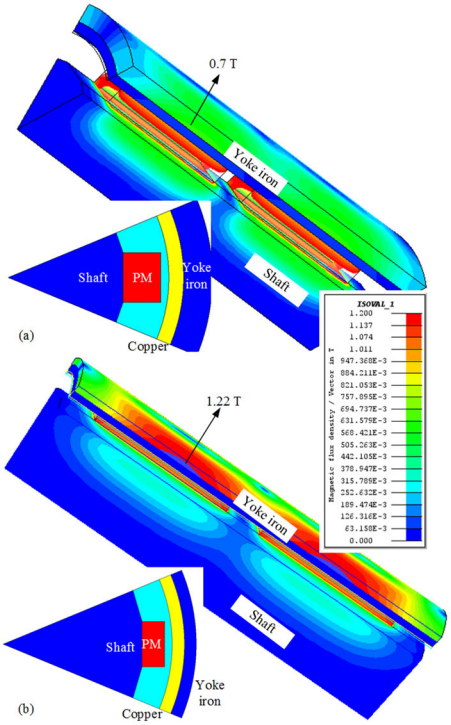

FIGURE 13. 2D view and 3D magnetic flux density distribution of (a) reference and (b) optimized PM-ECB.

TABLE 4. Comparison of the reference and the optimized PM-ECB.

	Reference model	Optimized model by quasi-3D analytical approach	% Difference
Total PM mass	28.8 g	17.32 g	-40%
Rated braking torque, T_{br}	0.146 Nm	0.144 Nm	+1%
Yoke mgn. flux density	0.7 T	1.18 T	+69%
Copper thickness, h_{Cu}	1.17 mm	1.05 mm	-10%
Yoke thickness	2.3 mm	1 mm	-57%
Cost	\$1,14	\$0,69	-40%

40% lower total PM mass, a 10% lower copper volume, and a 57% lower yoke volume with nearly the same rated braking torque. With the optimized brake, a 40% cost reduction could be achieved compared with the reference eddy current brake. The improvement percentage in the optimized design also is in harmony with the recently published papers about the optimization of ECBs [32], [33]. Nearly same reduction on the total mass and increase on braking torque are achieved in those studies. It has to be emphasized that material cost is used in the calculations. To defend the original design, we emphasize that standard copper tube was used in the design, whereas the optimization results were obtained with special copper tube.

The reference eddy-current brake was attached to the shaft of a drive motor (battery drilling machine). Certain speed was given to drive drill to rotate the eddy current brake.

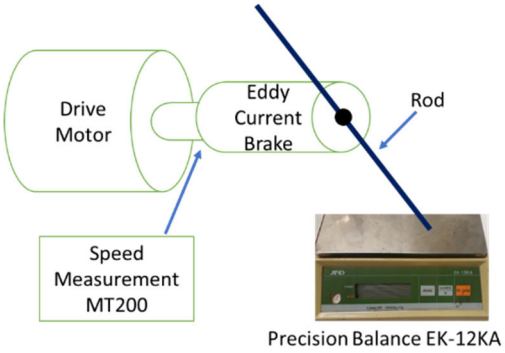

FIGURE 14. Test setup: The reference eddy-current brake is attached to the shaft of a drive motor and balance meter data is utilized to solve torque.

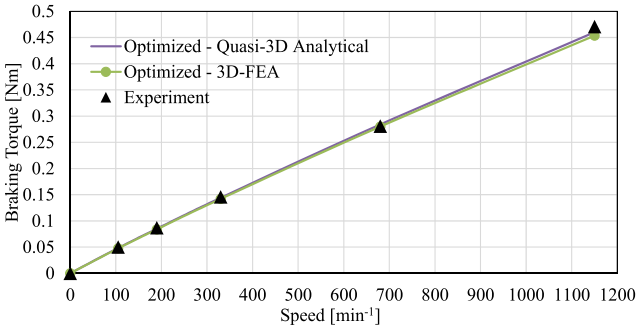

FIGURE 15. Comparison of the braking torque results obtained from the quasi-3D analytical and 3D-FEA and experiments.

A rod was attached to eddy current brake and as the brake rotates the torque created by the brake pushes a rod against a balance meter. The reading of the precision balance meter was recorded, and the torque was calculated from it. The rod is mounted in the middle of the shaft for balance situation. The tests were conducted at room temperature, 22 °C. The measurement data were collected by hand and without data processing. A sketch of the test setup is given in Fig. 14. The braking torque obtained from the proposed quasi-3D analytical approach is given in Fig. 15 together with the 3D-FEA and experimental results. The results show that the proposed quasi-3D analytical approach is in agreement with the 3D-FEA and experimental results. Thus, the proposed quasi-3D modeling seems a trustworthy approach. Obviously, it can be used in the modeling and design of PM-ECBs of this kind.

B. DEMAGNETIZATION ANALYSIS

A demagnetization analysis was also carried out to verify that the proposed PM-ECB has no risk of demagnetization. Demagnetization may result from thermal issues, armature reaction, and a thin magnet geometry [31]. The temperature has a significant influence on demagnetization; however, it has to be remembered that the PM-ECB works only for seconds as a speed limiter, and thus, the thermal behavior can be neglected. Armature reaction is also an important issue as it may cause irreversible demagnetization when the

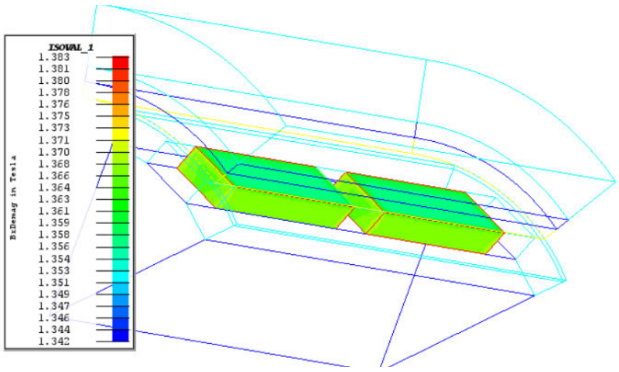

FIGURE 16. Demagnetization distribution of the proposed PM-ECB obtained by 3D-FEA.

PM-ECB has a thin magnet geometry and is made of a weak magnetic material. The worst design case for demagnetization at the speed of 1150 min^{-1} has a 5% reduction in the air-gap magnetic flux density compared with the zero speed. Therefore, it can be assumed that demagnetization is not a valid design objective in the optimization. The 3D-FEA simulation was carried out at the maximum operating speed, and the demagnetization distribution of the proposed PM-ECB is given in Fig. 16. The demagnetization was tracked in the transient analyses by computing the minimum flux density at each point in the magnet surface. The distribution shows that the proposed PM-ECB has no risk of demagnetization of the magnets.

VI. CONCLUSION

In this paper, an optimum design of a PM-ECB for the cost reduction of an industrial product was achieved by the MO-PSO based on nonlinear reluctance network modeling taking into account the armature reaction and the skin effect. The modified reluctance network modeling was presented by considering the actual structure of the PM-ECB as a quasi-3D analytical approach, and it was verified by the 3D-FEA and experiments. To reach an optimum design, multiobjective optimization was carried out by a particle swarm algorithm with three conflict parameters. The optimized design was selected by a 3D Pareto front, and the selection criteria were explained in detail. The optimized PM-ECB was verified by 3D-FEA and compared with the reference model, and it was shown that a significant reduction in the PM volume can be achieved with the optimized model at nearly the same braking torque. It was also shown that the model proposed in this paper can provide a 40% cost reduction with no risk of demagnetization of the magnets. For the future works, assumption of the tangential stress of the reference ECB can be increased for dimensioning the PM-ECB because the device did not warm up in the tests.

REFERENCES

[1] L. Pohjonen, "Roller shape with brake," U.S. Patent 0 245 018 A1, Aug. 25, 2016.
[2] Z. Mouton and M. J. Kamper, "Modeling and optimal design of an eddy current coupling for slip-synchronous permanent magnet wind generators," *IEEE Trans. Ind. Electron.*, vol. 61, no. 7, pp. 3367–3376, Jul. 2014.

[3] K. Karakoc, E. J. Park, and A. Suleman, "Improved braking torque generation capacity of an eddy current brake with time varying magnetic fields: A numerical study," *Finite Elements Anal. Des.*, vol. 59, pp. 66–75, Oct. 2012.
[4] A. H. C. Gosline and V. Hayward, "Eddy current brakes for haptic interfaces: Design, identification, and control," *IEEE/ASME Trans. Mechatronics*, vol. 13, no. 6, pp. 669–677, Dec. 2008.
[5] P. J. Wang and S. J. Chiueh, "Analysis of eddy-current brakes for high speed railway," *IEEE Trans. Magn.*, vol. MAG-34, no. 4, pp. 1237–1239, Jul. 1998.
[6] A. A. Adly and S. K. Abd-El-Hafiz, "Speed-Range-Based optimization of nonlinear electromagnetic braking systems," *IEEE Trans. Magn.*, vol. 43, no. 6, pp. 2606–2608, Jun. 2007.
[7] S. Anwar and B. Zheng, "An antilock-braking algorithm for an eddy-current-based brake-by-wire system," *IEEE Trans. Veh. Technol.*, vol. 56, no. 3, pp. 1100–1107, May 2007.
[8] D. Valderas, I. Mesa, I. Adin, H. Lehmann, G. Lancaster, O. Stark, W. Baldauf, and J. del Portillo, "Modeling eddy current brake emissions for electromagnetic compatibility with signaling devices in high-speed railways," *IEEE Trans. Veh. Technol.*, vol. 66, no. 11, pp. 9743–9752, Nov. 2017.
[9] E. M. Pribonic and M. T. Thompson, "Permanent magnet eddy brake with flux-steering poles," U.S. Patent 6 523 650 B1, Feb. 25, 2003.
[10] S. Bouissou, "Eddy current retarder," U.S. Patent 6 700 265 B1, Mar. 2, 2004.
[11] M. Gulec, E. Yolacan, and M. Aydin, "Design, analysis and real time dynamic torque control of single-rotor–single-stator axial flux eddy current brake," *IET Electr. Power Appl.*, vol. 10, no. 9, pp. 869–876, Nov. 2016.
[12] S. Cho, H. Liu, H. Ahn, J. Lee, and H. Lee, "Eddy current brake with a two-layer structure: Calculation and characterization of braking performance," *IEEE Trans. Magn.*, vol. 53, no. 11, May 2017, Art. no. 8110205.
[13] R. Yazdanpanah and M. Mirsalim, "Hybrid electromagnetic brakes: Design and performance evaluation," *IEEE Trans. Energy Convers.*, vol. 30, no. 1, pp. 60–69, Mar. 2015.
[14] L. Ye, D. Li, Y. Ma, and B. Jiao, "Design and performance of a water-cooled permanent magnet retarder for heavy vehicles," *IEEE Trans. Energy Convers.*, vol. 26, no. 3, pp. 953–958, Sep. 2011.
[15] S. E. Gay and M. Ehsani, "Parametric analysis of eddy-current brake performance by 3-D finite-element analysis," *IEEE Trans. Magn.*, vol. 42, no. 2, pp. 319–328, Feb. 2006.
[16] K.-H. Shin, H.-I. Park, H.-W. Cho, and J.-Y. Choi, "Semi-Three-Dimensional analytical torque calculation and experimental testing of an eddy current brake with permanent magnets," *IEEE Trans. Appl. Supercond.*, vol. 28, no. 3, pp. 1–5, Apr. 2018.
[17] J. Wang and J. Zhu, "A simple method for performance prediction of permanent magnet eddy current couplings using a new magnetic equivalent circuit model," *IEEE Trans. Ind. Electron.*, vol. 65, no. 3, pp. 2487–2495, Mar. 2018.
[18] K. Hori, D. Mochizuki, Y. Kikuchi, H. Wakiwaka, M. Sonehara, and T. Sato, "Fundamental study of eddy current brakes by using magnetic clad material," in *Proc. Int. Conf. Electr. Mach. (ICEM)*, Aug. 2020, pp. 1651–1656.
[19] N. Takahashi, M. Natsumeda, K. Muramatsu, C. Yamada, M. Ogawa, S. Kobayashi, and T. Kuwahara, "Optimization of permanent magnet type of retarder using 3-D finite element method and direct search method," *IEEE Trans. Magn.*, vol. 34, no. 5, pp. 2996–2999, Sep. 1998.
[20] S. Sharif, J. Faiz, and K. Sharif, "Performance analysis of a cylindrical eddy current brake," *IET Electr. Power Appl.*, vol. 6, no. 9, pp. 661–668, Nov. 2012.
[21] J. Pyrhánen, T. Jokinen, and V. Hrabovcova, *Design of Rotating Electrical Machines*. Chichester, U.K.: Wiley, 2008.
[22] C. Bruzzese, D. Zito, and A. Tessarolo, "Finite reluctance approach: A systematic method for the construction of magnetic network-based dynamic models of electrical machines," in *Proc. AEIT Annu. Conf.-From Res. Ind.*, Sep. 2014, pp. 1–6.
[23] J. Perho, "Reluctance network for analysing induction machines," Ph.D. dissertation, Dept. Elect. and Commun. Eng., Helsinki Univ. Tech., Espoo, Finland, 2002.
[24] A. Boehm and I. Hahn, "Measurement of magnetic properties of steel at high temperatures," in *Proc. 40th Annu. Conf. Ind. Electron. Soc.*, Oct. 2014, pp. 715–721.
[25] J. Tian, D. Li, K. Ning, and L. Ye, "A timesaving transient magneto-thermal coupling model for the eddy current brake," *IEEE Trans. Veh. Technol.*, vol. 69, no. 10, pp. 10832–10841, Oct. 2020.
[26] J. Pyrhonen, V. Ruuskanen, J. Nerg, J. Puranen, and H. Jussila, "Permanent-magnet length effects in AC machines," *IEEE Trans. Magn.*, vol. 46, no. 10, pp. 3783–3789, Oct. 2010.
[27] J. Pyrhonen, J. Nerg, P. Kurronen, and U. Lauber, "High-speed high-output solid-rotor induction-motor technology for gas compression," *IEEE Trans. Ind. Electron.*, vol. 57, no. 1, pp. 272–280, Jan. 2010.
[28] J. Kennedy and R. Eberhart, "Particle swarm optimization," in *Proc. IEEE Int. Conf. Neural Netw.*, vol. 4, Nov. 1995, pp. 1942–1948.
[29] C. A. C. Coello, G. T. Pulido, and M. S. Lechuga, "Handling multiple objectives with particle swarm optimization," *IEEE Trans. Evol. Comput.*, vol. 8, no. 3, pp. 256–279, Jun. 2004.
[30] N. Ryu, S. Lim, S. Min, K. Izui, and S. Nishiwaki, "Multi-objective optimization of magnetic actuator design using adaptive weight determination scheme," *IEEE Trans. Magn.*, vol. 53, no. 6, Jun. 2017, Art. no. 7205104.
[31] N. Bianchi and H. Mahmoud, "An analytical approach to design the PM in PMAREL motors robust toward the demagnetization," *IEEE Trans. Energy Convers.*, vol. 31, no. 2, pp. 800–809, Jun. 2016.
[32] L. Ye, Y. Liu, and D. Li, "Performance analysis and optimization of liquid-cooled and flywheel-type eddy current retarder," *IEEE Trans. Magn.*, vol. 55, no. 6, Jun. 2019, Art. no. 8001005, doi: 10.1109/TMAG.2019.2894771.
[33] R. Tarvirdilu Asl, H. M. Yáksel, and O. Keysan, "Multi-objective design optimization of a permanent magnet axial flux eddy current brake," *TURKISH J. Electr. Eng. Comput. Sci.*, pp. 998–1011, Mar. 2019.